

Parameter calculation and result storage for phase-field simulation in α-Mg dendrite growth of Mg-5-wt% Zn alloy

Wei-Peng Chen(陈伟鹏), Hua Hou(侯华), Yun-Tao Zhang(张云涛), Wei Liu(柳伟), and Yu-Hong Zhao(赵宇宏)
Citation: Chin. Phys. B, 2023, 32 (**11**): 118103. DOI: 10.1088/1674-1056/acd7e3
Journal homepage: http://cpb.iphy.ac.cn; http://iopscience.iop.org/cpb

What follows is a list of articles you may be interested in

GPU parallel computation of dendrite growth competition in forced convection using the multi-phase-field-lattice Boltzmann model

Zi-Hao Gao(高梓豪), Chang-Sheng Zhu(朱昶胜), and Cang-Long Wang(王苍龙)
Chin. Phys. B, 2023, 32 (**7**): 078101. DOI: 10.1088/1674-1056/acbc68

Amorphous transformation of ternary $Cu_{45}Zr_{45}Ag_{10}$ alloy under microgravity condition

Ming-Hua Su(苏明华), Fu-Ping Dai(代富平), and Ying Ruan(阮莹)
Chin. Phys. B, 2022, 31 (**9**): 098106. DOI: 10.1088/1674-1056/ac67c9

Phase-field study of spinodal decomposition under effect of grain boundary

Ying-Yuan Deng(邓英远), Can Guo(郭灿), Jin-Cheng Wang(王锦程), Qian Liu(刘倩), Yu-Ping Zhao(赵玉平), and Qing Yang(杨卿)
Chin. Phys. B, 2021, 30 (**8**): 088101. DOI: 10.1088/1674-1056/abea9b

A lattice Boltzmann-cellular automaton study on dendrite growth with melt convection in solidification of ternary alloys

Dong-Ke Sun(孙东科), Zhen-Hua Chai(柴振华), Qian Li(李谦), Guang Lin(林光)
Chin. Phys. B, 2018, 27 (**8**): 088105. DOI: 10.1088/1674-1056/27/8/088105

Effects of physical parameters on the cell-to-dendrite transition in directional solidification

Wei Lei (魏雷), Lin Xin (林鑫), Wang Meng (王猛), Huang Wei-Dong (黄卫东)
Chin. Phys. B, 2015, 24 (**7**): 078108. DOI: 10.1088/1674-1056/24/7/078108

Parameter calculation and result storage for phase-field simulation in α-Mg dendrite growth of Mg-5-wt% Zn alloy

Wei-Peng Chen(陈伟鹏)[1], Hua Hou(侯华)[1,3], Yun-Tao Zhang(张云涛)[1], Wei Liu(柳伟)[1], and Yu-Hong Zhao(赵宇宏)[2,1,4,†]

[1] *School of Materials Science and Engineering, Collaborative Innovation Center of Ministry of Education and Shanxi Province for High-performance Al/Mg Alloy Materials, North University of China, Taiyuan* 030051, *China*
[2] *Beijing Advanced Innovation Center for Materials Genome Engineering, University of Science and Technology Beijing, Beijing* 100083, *China*
[3] *School of Materials Science and Engineering, Taiyuan University of Science and Technology, Taiyuan* 030024, *China*
[4] *Institute of Materials Intelligent Technology, Liaoning Academy of Materials, Shenyang* 110004, *China*

(Received 2 February 2023; revised manuscript received 25 April 2023; accepted manuscript online 23 May 2023)

Parameter calculation and result storage, as two necessary steps in phase-field simulation play an important role in ensuring the accuracy of simulation results. A strategy of parameter calculation and result storage is presented for phase-field simulation in α-Mg dendrite growth of Mg-5-wt% Zn alloy under isothermal solidification. Based on the phase diagram and empirical formulas, key parameters of the phase-field model, such as equilibrium partition coefficient k, liquidus slope m, solutal diffusion coefficient in liquid D_l, and solutal diffusion coefficient in solid D_s, can be obtained. Both structured grid method and structured point method can be used to store simulation results, but using the latter method will reduce about 60% storage space and 37.5% storage time compared with the former. Finally, convergent simulation results of α-Mg dendrite growth are obtained and they are in good agreement with the experimental results about optical micrograph, which verify the accuracy of parameters and stability of storage method.

Keywords: parameter calculation, result storage, phase-field method, dendrite growth

PACS: 81.30.Fb, 81.10.Aj **DOI:** 10.1088/1674-1056/acd7e3

1. Introduction

The microstructures formed in solidification play a significant role in process control and mechanical properties of the final casting.[1] Dendrite, as a typical solidification microstructure, exists in most metallic alloys.[2,3] Understanding the evolution of dendrite morphologies and segregation distribution is important in controlling final microstructures. With the development of computer science and material thermodynamics, the phase-field method has become an indispensable means to simulate the evolution of microstructures, especially dendrites.[4–8]

Typically, a comprehensive phase-field simulation process involves several steps: modeling, parameter calculation, equations solver, and result storage and post-processing. In recent years, a lot of efforts have been made to model and making a equation solver. For example, in terms of modeling, multiphase and multiscale[9,10] and phase-field-lattice Boltzmann[11] models have been developed, and in terms of making equation solver, adaptive mesh refinement[12,13] and parallel computing[14,15] methods have been presented. Nevertheless, compared with the above two steps, calculating parameters, and result storage and post-processing were often only briefly mentioned in most of published papers.[16–18] There have been almost no systematic studies for the latter two steps, which will limit the application of the phase-field method. Moreover, according to Tourret *et al.*,[19] the energy function at the core of phase-field model depends on a large number of parameters that control different energy contributions, and quantitative predictions of microstructure evolution require careful identification of parameters. Therefore, it is necessary to find a feasible strategy for parameter calculation, which will improve the accuracy of simulation results. A natural link exists between phase-field method and CalPhaD method, and the phase diagram and thermodynamic/kinetic data of alloys can be obtained through the CalPhaD method.[20] For alloy solidification, an accurate description of solutal diffusion in liquid and solid is helpful in accurately predicting the segregation distribution.[21,22] According to empirical formulas from experiments or theoretical calculations, solutal diffusion coefficient in liquid and solid can be obtained, which are essential to describe solute diffusion. Then, key parameters of the phase-field model can be presented by combining the CalPhaD method and empirical formulas. In addition, a feasible result storage strategy requires not only high storage efficiency but also convenient post-processing. Since the simulation domain in phase-field simulation is usually a regular graph, finite difference[23] and finite volume[24] methods are often used to solve equations. Therefore, it is reasonable to use structured grid or structured point storage

†Corresponding author. E-mail: zhaoyuhong@nuc.edu.cn
© 2023 Chinese Physical Society and IOP Publishing Ltd

methods for result storage.

In this study, a method of calculating parameters and storing results is presented for phase-field simulation in α-Mg dendrite growth of Mg-5-wt% Zn alloy under isothermal solidification. Based on the PANDAT software, the Mg–Zn phase diagram is calculated, then third-order polynomials are adapted to fit both solidus and liquidus lines, and parameters such as equilibrium partition coefficient k, liquidus slope m are obtained. Subsequently, the solutal diffusion coefficient in liquid D_l and solutal diffusion coefficient in solid D_s are calculated from empirical formulas. The structured grid and structured point storage methods are chosen to store simulation results, and the storage efficiencies of the two methods are compared. Finally, α-Mg dendrite growth is studied to test the accuracy of parameters and stability of storage methods.

The rest of this paper is organized as follows. The phase-field method is introduced in Section 2. The results and analysis are given in Section 3, and the discussion is presented in Section 4. Finally, conclusions are drawn from the present study in Section 5.

2. Phase-field method

2.1. Phase-field equations

In this study, a quantitative phase-field model is used to describe α-Mg dendrite growth of Mg-5-wt% Zn alloy under isothermal solidification.[25,26] The phase-field is represented by ϕ, with $\phi=+1$ in the solid, $\phi=-1$ in the liquid, and ϕ varying smoothly from $+1$ to -1 within the diffuse interface. For a two-phase system, the free energy function can be described as

$$F[\phi,c,T] = \int_{\mathrm{d}V}\left[\frac{\sigma}{2}|\nabla\phi|^2+f(\phi,T_\mathrm{m}) + f_\mathrm{AB}(\phi,c,T)\right], \tag{1}$$

where c is the solute concentration, T is the temperature, σ is the energy per unit length, and T_m is the melting temperature. The double-well potential and free energy density functions are given, respectively, by

$$f(\phi,T_\mathrm{m}) = H\left(-\phi^2/2+\phi^4/4\right), \tag{2}$$

$$f_\mathrm{AB}(\phi,c,T) = f^\mathrm{A}(T_\mathrm{m})-(T-T_\mathrm{m})s(\phi) + \frac{RT_\mathrm{m}}{v_0}(clnc-c)+\varepsilon(\phi)c, \tag{3}$$

where H is the barrier height, $f^\mathrm{A}(T_\mathrm{m})$ is the free energy for pure A at T_m, R is the gas constant, v_0 is the molar volume of A, $s(\phi)$ and $\varepsilon(\phi)$ are interpolation functions related to entropy density and internal energy density, respectively. According to Allen–Cahn equation and Cahn–Hilliard equation, the variational formulation for all fields can be derived from

$$\frac{\partial\phi}{\partial t} = -M_\phi\frac{\delta F}{\delta\phi}, \tag{4}$$

$$\frac{\partial c}{\partial t} = \nabla\cdot\left(M_\mathrm{c}\nabla\frac{\delta F}{\delta c}\right), \tag{5}$$

where M_ϕ and M_c are the mobility related to the interfacial kinetic coefficient and solute diffusion coefficient, respectively. The evolution equation for ϕ is given as follows:

$$\begin{aligned}&[1+(1-k)U]a_\mathrm{s}^2(\boldsymbol{n})\frac{\partial\phi}{\partial t}\\ &= \nabla\cdot\left[a_\mathrm{s}^2(\boldsymbol{n})\nabla\phi\right]+\sum_{\eta=x,y,(z)}\frac{\partial}{\partial\eta}\left[|\nabla\phi|^2 a_\mathrm{s}(\boldsymbol{n})\frac{\partial a_\mathrm{s}(\boldsymbol{n})}{\partial(\partial\phi/\partial\eta)}\right]\\ &\quad+\left(1-\phi^2\right)\left[\phi-\lambda\left(1-\phi^2\right)U\right],\end{aligned} \tag{6}$$

where k is the equilibrium partition coefficient and λ is the coupling parameter of time and space. The anisotropy function for two-dimensional simulations is $a_\mathrm{s}(\boldsymbol{n}) = 1+\varepsilon_0+\varepsilon_6\cos[6(\varphi-\varphi_0)]$, and for three-dimensional simulations is $a_\mathrm{s}(\boldsymbol{n}) = 1+\varepsilon_1\left(3\cos^2\theta-1\right)^2+\varepsilon_2\left(\sin^3\theta\cos^3\varphi-3\sin^3\theta\sin^2\varphi\cos\varphi\right)^2\left(9\cos^2\theta-1-\varepsilon_3\right)^2$,[27] where $\theta\in[0,\pi]$ and $\varphi\in[0,2\pi]$ are the spherical coordinate angles, φ_0 is the misorientation angle, ε_0, ε_1, ε_2, ε_3, and ε_6 are the magnitudes of crystal anisotropy, $\boldsymbol{n}=-\nabla\phi/|\nabla\phi|$ is the unit vector normal to the interface. The dimensionless solute concentration U is given as follows:

$$U = \frac{1}{1-k}\left[\frac{2c/c_\mathrm{l}^0}{(1+k)-(1-k)\phi}-1\right], \tag{7}$$

where c_l^0 is the liquid concentration at the equilibrium temperature T_0. The evolution equation for U is given as follows:

$$\begin{aligned}&\left(\frac{1+k}{2}-\frac{1-k}{2}\phi\right)\frac{\partial U}{\partial t}\\ &= \nabla\cdot[Dq(\phi)\nabla U-\boldsymbol{j}_\mathrm{at}]+\frac{1}{2}[1+(1-k)U]\frac{\partial\phi}{\partial t},\end{aligned} \tag{8}$$

where $D=D_\mathrm{l}\tau_0/W_0^2$ is the dimensionless solutal diffusion coefficient, D_l is the solutal diffusion coefficient in liquid, $\tau_0=\alpha_2\lambda W_0^2/D_\mathrm{l}$ is the relaxation time, $W_0=d_0\lambda/\alpha_\mathrm{l}$ is the interface thickness, $d_0=\Gamma/\Delta T_0$ is the chemical capillary length, $\Gamma=\gamma_0 T_\mathrm{m}/(\rho L_\mathrm{f})$ is the Gibbs–Thomson coefficient, γ_0 is the surface energy of the solid-liquid interface, ρ is the density of the pure A, L_f is the latent heat of fusion, $\Delta T_0=|m|(1-k)c_\mathrm{l}^0$ is the equilibrium freezing temperature range, m is the liquidus slope, $\alpha_\mathrm{l}=0.8839$ and $\alpha_2=0.6267$ are constants, $q(\phi)=(1-\phi)/2+kD_\mathrm{s}(1+\phi)/(2D_\mathrm{l})$ is the interpolating function, $\boldsymbol{j}_\mathrm{at}=-1/(2\sqrt{2})(1-kD_\mathrm{s}/D_\mathrm{l})[1+(1-k)U](\partial\phi/\partial t)(\nabla\phi/|\nabla\phi|)$ is the anti-trapping current, and D_s is the solutal diffusion coefficient in solid.

In this study, the noise of $n_0\chi\sqrt{\Delta t}\left(1-\phi^2\right)$ is added to ϕ at each point and each time step, therefore, at the next time step, it can be expressed as follows:[28]

$$\phi^{t+\Delta t}=\phi^t+\Delta t\frac{\partial\phi^t}{\partial t}+n_0\chi\sqrt{\Delta t}\left[1-\left(\phi^t\right)^2\right], \tag{9}$$

where χ is a random number generated with a flat distribution in the range from -1 to $+1$, n_0 is the magnitude of the noise, and the term $\left[1-(\phi^t)^2\right]$ keeps the noise localized in the vicinity of the interface where $\phi\neq\pm1$.

2.2. Computational conditions

The finite volume method is used to discretize Eqs. (6) and (8). The Neumann boundary with zero fluxes is applied to the phase-field model and therefore there is no solute flux across the boundaries. The sphere nucleation seed radius is set to $r_0=5.0\Delta x$. The supersaturation of the melt is $\Omega=\left(c_l^0-c_0\right)/\left[c_l^0(1-k)\right]$, which corresponds to the fixed undercooling $\Delta T=T_m-T_0$, where c_0 is the initial solute concentration far from the solid-liquid interface. The initial phase-field order parameter is set to $\phi(\boldsymbol{r},0)=-\tanh\left[(\boldsymbol{r}-\boldsymbol{r}_0)/\sqrt{2}\right]$, dimensionless solute concentration is set to $U(\boldsymbol{r},0)=-\Omega$. This study is based on the solidification module in EasyPhase software, which is a comprehensive phase-field theory software package developed by the group of Prof. Yuhong Zhao.

3. Results and analysis

3.1. Key parameters calculation

According to Eqs. (6)–(8), the key parameters of the phase-field model contain equilibrium partition coefficient k, solutal diffusion coefficient in liquid D_l, solutal diffusion coefficient in solid D_s, and chemical capillary length d_0. The above parameters are the bridge between the phase-field model and the solidification process, playing an important role in determining the accuracy of simulation results. Based on thermodynamic data from PANDAT software (Version 2021b 64bit), part of the Mg–Zn phase diagram is calculated as shown in Fig. 1. To obtain accurate physical parameters, the third-order polynomials are adapted to fit both solidus and liquidus lines as follows:[29]

$$T_l(c)=a_1c^3+b_1c^2+c_1c+T_m, \tag{10}$$

$$T_s(c)=a_2c^3+b_2c^2+c_2c+T_m, \tag{11}$$

where $a_1=-0.0006$, $b_1=-0.0212$, $c_1=-3.0005$, $a_2=1.5425$, $b_2=-1.6070$, $c_2=-57.9819$, and $T_m=923$ K. For the given equilibrium temperature $T_0=T_l=T_s=889$ K, corresponding liquid concentration $c_l^0=10.3524$ wt% and solid concentration $c_s^0=0.5818$ wt%, therefore, the equilibrium partition coefficient $k=c_s^0/c_l^0=0.0562$. In addition, the liquidus slope for the concentration c_l^0 can be obtained from $m=(\partial T_l/\partial c)_{c=c_l^0}=3a_1\left(c_l^0\right)^2+2b_1c_l^0+c_1=-3.6324$ K/wt%, so the chemical capillary length $d_0=0.3308\times10^{-7}$ m.

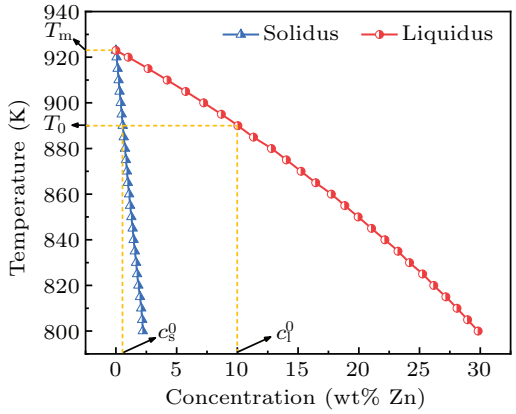


Fig. 1. Part of Mg–Zn phase diagram, with points representing the data available from thermodynamic database, and lines referring to solidus and liquidus lines via the third-order polynomials approximate.

According to the empirical formulas,[30–32] the solutal diffusion coefficient in liquid and solid can be expressed, respectively, as

$$D_l=\frac{k_BT^{1/2}}{4\pi}\frac{\left(\rho^m_{solute}\right)^{1/3}}{0.644\times10^{-8}\left(M_{solute}\right)^{1/3}\left(1-0.112\sqrt{T/T^m_{solute}}\right)}\cdot\frac{\left(V_{solvent}\right)^{2/3}}{\hat{A}\left(M_{solvent}\right)^{1/2}}\cdot T\exp\left(-\hat{B}\frac{T^m_{solvent}}{T}\right), \tag{12}$$

$$D_s=D_0\exp(-Q/RT), \tag{13}$$

where $\hat{A}$ and $\hat{B}$ are both the adjustment constant, k_B is the Boltzmann constant, ρ^m_{solute} is the density of solute at the melting temperature T^m_{solute}, M_{solute} is the atomic mass of solute, the terms $V_{solvent}$, $M_{solvent}$, and $T^m_{solvent}$ are the absolute molar volume, the atomic mass, and the melting temperature of the solvent, respectively. Moreover, D_0 is the pre-exponential factor, and Q is the activation energy. For Mg–Zn alloy, the Mg substrate is regarded as the solvent, and alloying element Zn is regarded as the solute. Therefore, according to Eqs. (12) and (13), the solutal diffusion coefficient in liquid is $D_l=4.6763\times10^{-9}$ m^2/s and solutal diffusion coefficient in solid is $D_s=5.1899\times10^{-14}$ m^2/s at the temperature $T=T_0$.

Moreover, Becker *et al.*[33] showed that the simulations converge to stationary results for $W_0/d_0\leq10$, therefore, $W_0=9.0d_0=2.9772\times10^{-7}$ m, coupling constant $\lambda=7.9551$, relaxation time $\tau_0=9.4497\times10^{-5}$ s, space step size $\Delta x=0.8W_0=2.3818\times10^{-7}$ m, and time step size $\Delta t=0.01\tau_0=9.4497\times10^{-7}$ s. The other physical and model parameters for phase-field simulations are listed in Table 1.[34–36]

Table 1. Physical and model parameters for phase-field simulations.

Parameter	Value
Surface energy, γ_0	0.81 J/m^2
Density, ρ	1740 kg/m^3
Latent heat of fusion, L_f	3.66×10^5 J/kg
Pre-exponential factor, D_0	0.0483×10^{-5} m^2/s
Activation energy, Q	1.186×10^5 J/mol
Initial concentration, c_0	5.0 wt%
Supersaturation, Ω	0.55
Anisotropy strength, ε_0, ε_6, ε_1, ε_2, ε_3	0.01, 0.06, –0.02, 0.15, 0.0
Simulation domain, Λ	$400\Delta x \times 400\Delta x\,(\times 400\Delta x)$

3.2. Structured grid and structured point storage

Usually, the results of the phase-field simulation are stored in the array and need to be visualized by post-processing software or package. Choosing an appropriate storage strategy is not only beneficial to the post-processing of results but also able to save storage space. In this study, based on the *.vtk* file format, the structured grid method and structured point method are used to store simulation results. Figure 2(a) shows the structured grid storage method. It can be found that the grid needs first to be built according to the size of the array, and the elements in the array are then stored in grid nodes. Figure 2(b) shows the structured point storage method, which is different from the structured grid: elements in the array are directly stored as nodes. Figures 2(c) and 2(d) show simulation results stored by using the structured grid method and structured point method, respectively, through post-processing software: Paraview-Version 5.6.0 64bit. It can be found that in terms of the resolution of this study, there is almost no difference in dendrite morphologies obtained by these two storage methods. Moreover, for structured grid storage, when elements in the array are sequentially stored in grid nodes, undistorted post-processing results can be obtained only when the total number of nodes in each of all directions of the simulation domain is similar. When elements in the array are stored in reverse order in grid nodes, undistorted post-processing results can be obtained unconditionally. For structured point storage, undistorted post-processing results can be obtained only when elements in the array are stored in reverse order in nodes.

To illustrate the efficiency of the structured grid storage method and structured point storage method, storage space and storage time varying with node number are counted as shown in Fig. 3. With the increase of node number, both storage space and storage time will increase linearly. For structured grid storage, the relationship between storage space and node number satisfies $y = 15.0 \times 10^{-6}x$, and the relationship between storage time and node number complies with $y = 0.8 \times 10^{-6}x$. For the structured point storage, the relationship between storage space and node number meets $y = 6.0 \times 10^{-6}x$, and the relationship between storage time and node number obeys $y = 0.5 \times 10^{-6}x$. Therefore, using the structured point storage method will reduce about 60% storage space and 37.5% storage time compared with the structured grid storage method. When the node number is small, the storage advantage of the structured point over the structured grid method is not significant. However, when the node number is large, it is difficult to obtain post-processing results even based on the current computer level. Therefore, when carrying out large-scale computing, especially for three-dimensional simulation, the use of the structured point storage method will greatly reduce storage space and time.

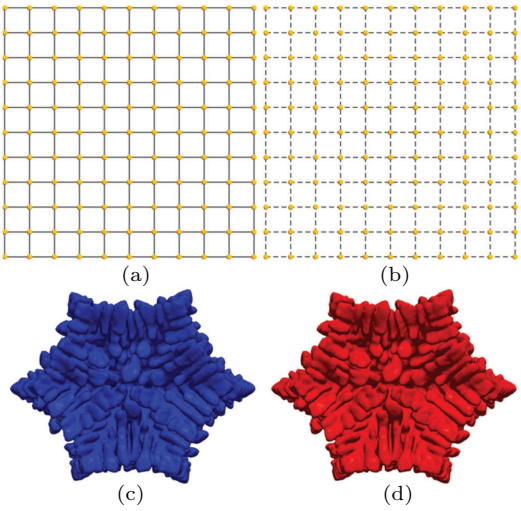


Fig. 2. (a) Schematic diagram of structured grid storage and (b) structured point storage. Simulated morphologies of α-Mg dendrite of Mg-5-wt% Zn alloy under isothermal solidification at $t = 6000\Delta t$ by using (c) structured grid method and (d) structured point method.

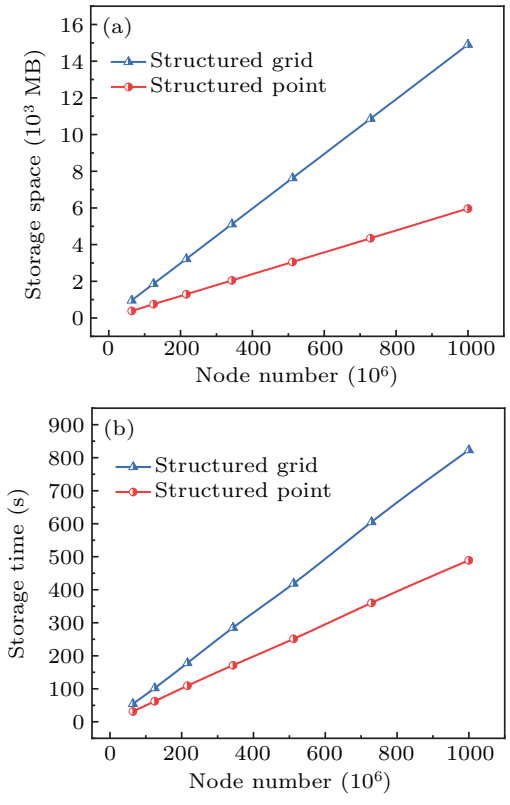


Fig. 3. Storage space and storage time varying with node number.

4. Discussion

4.1. The α-Mg dendrite growth

To verify the accuracy of parameters and stability of storage methods, the phase-field simulation in α-Mg dendrite growth of Mg-5-wt% Zn alloy is investigated. Figure 4 shows solute field evolution in the whole simulation domain, it can be found that the dendrite on $\{0001\}$ crystal plane has six primary dendrite arms, showing a typical snowflake morphology, which result from the solid–liquid interface anisotropy. Owing to solute redistribution during the growth of α-Mg dendrite, the solute is enriched on the liquid side of the solid–liquid interface, and solute enrichment at the root of the dendrite is higher than that at the tip of the dendrite, which results from curvature effect. Figure 5 shows the solute field evolution at the solid–liquid interface, it can be found that the three-dimensional dendrite has eighteen primary dendrite arms, the six primary dendrite arms on $\{0001\}$ crystal plane grows along the $\langle 11\bar{2}0\rangle$ direction, while the other twelve primary dendrite arms grow along the $\langle 11\bar{2}3\rangle$ direction, and the growth velocity of the primary dendrite arm growing along the $\langle 11\bar{2}0\rangle$ direction is faster than that along the $\langle 11\bar{2}3\rangle$ direction. Moreover, there is also a concentration difference at the solid–liquid interface, the concentration is high in depression areas and low in uplift areas, and the difference in concentration between the two areas is about 0.2, which is lower than that between solid and liquid.

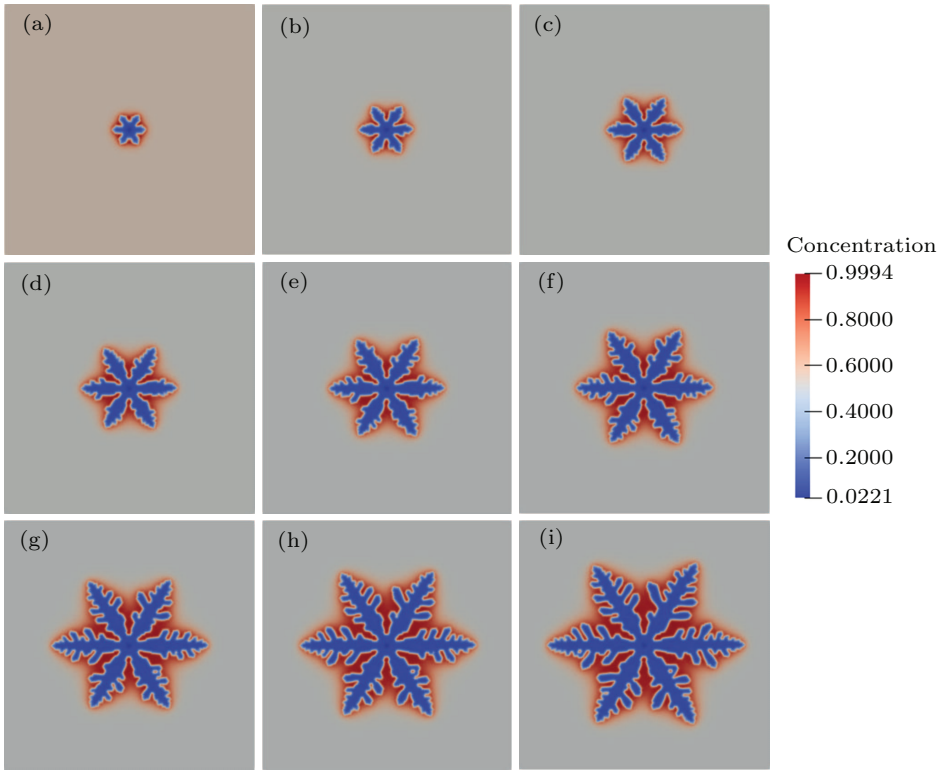


Fig. 4. Solute field evolution in α-Mg dendrite growth of Mg-5-wt% Zn alloy under isothermal solidification in the whole simulation domain at $t = 1000\Delta t$ (a), $2000\Delta t$ (b), $3000\Delta t$ (c), $4000\Delta t$ (d), $5000\Delta t$ (e), $6000\Delta t$ (f), $7000\Delta t$ (g), $8000\Delta t$ (h), and $9000\Delta t$ (i).

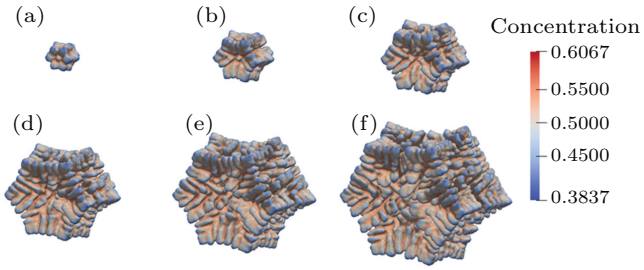


Fig. 5. Solute field evolution in α-Mg dendrite growth of Mg-5-wt% Zn alloy under isothermal solidification at solid–liquid interface and $t = 1000\Delta t$ (a), $2000\Delta t$ (b), $3000\Delta t$ (c), $4000\Delta t$ (d), $5000\Delta t$ (e), and $6000\Delta t$ (f).

Figure 6 shows the evolutions of solid fraction, dendrite tip velocity, and dendrite tip radius in α-Mg dendrite growth of Mg-5-wt% Zn alloy under isothermal solidification. With dendrite growth, solid fraction increases nonlinearly and the slope of the curve increases gradually, which result from the development of sidebranching. Moreover, since the curve is smooth, the random distribution of sidebranching will not cause a large fluctuation of solid fraction. To avoid the effect of excessive noise on the dendrite tip stability, the magnitude of the noise is set to $n_0 = 0$ when calculating the dendrite tip velocity and radius. With dendrite growth, dendrite tip velocity will first increase from 0 to 2.56 and then decrease gradually and stabilize at about 2.24. While the dendrite tip radius will increase gradually, from 0 to 2.2, and stabilize at about 2.2.

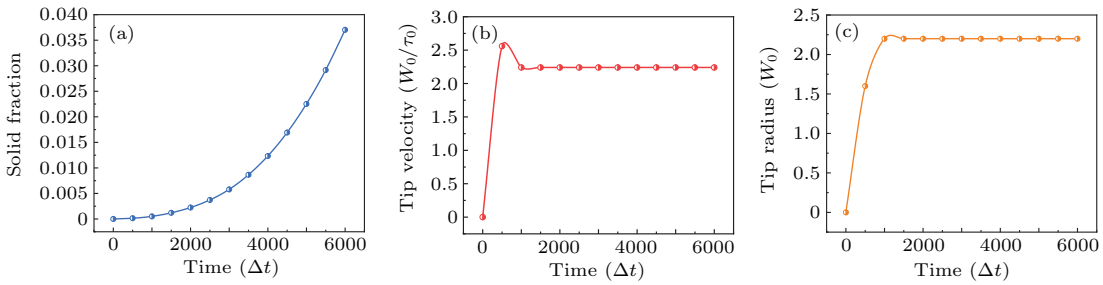


Fig. 6. Time evolution of (a) solid fraction, (b) dendrite tip velocity, and (c) dendrite tip radius in α-Mg dendrite growth of Mg-5-wt% Zn alloy under isothermal solidification.

4.2. Experimental validation

To verify the accuracy of simulations, simulation results are compared with experimental results as shown in Fig. 7. The original ingots with a nominal composition of Mg-5-wt% Zn are fabricated in an electric-resistant furnace under an argon atmosphere by melting high-purity Mg, and Zn at 750 °C. Then, the melts are cast into a preheated mold at 200 °C when the temperature decreases to 730 °C, and the cast alloys each with a diameter of 42 mm and a height of 150 mm are obtained. It can be found that both morphologies of α-Mg dendrite of experimental and simulation results on the $\{0001\}$ crystal plane have six primary dendrite arms and develop secondary dendrite arms. The angle between the primary dendrite arms is 60°, and the angle between the primary dendrite arms and secondary dendrite arms is also 60°, therefore, the growth direction of primary dendrite arms and secondary dendrite arms are both $\langle 11\bar{2}0\rangle$. Moreover, it can be found that the morphologies of α-Mg dendrite of experimental and simulation results on $\{11\bar{2}1\}$ crystal plane have both four primary dendrite arms and undeveloped secondary dendrite arms. The angle between the left primary dendrite arm and the right primary dendrite arm is about 85°, and the angle between the upper primary dendrite arm and the lower primary dendrite arm is about 95°. The growth direction of primary dendrite arm is $\langle 11\bar{2}3\rangle$, and since the interaction between secondary dendrite arms, their growth direction will be slightly deflected.

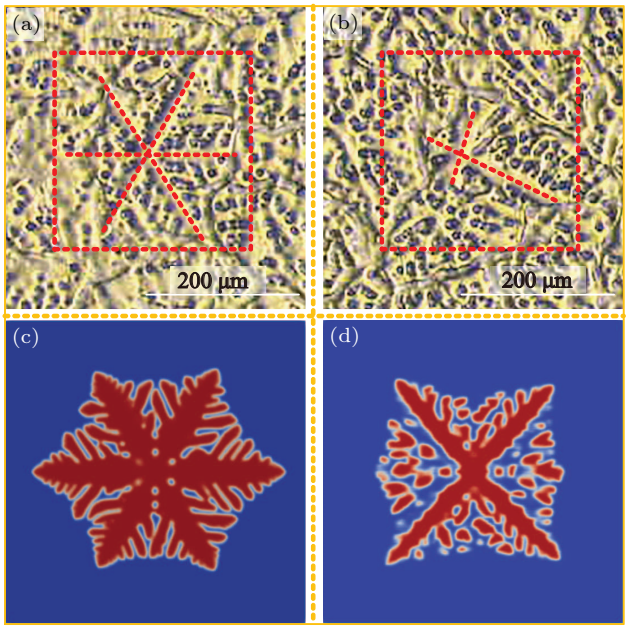


Fig. 7. Optical micrographs of α-Mg dendrite of as-cast Mg-5-wt% Zn alloy under air cooling on (a) $\{0001\}$ crystal plane and (b) $\{11\bar{2}1\}$ crystal plane, and morphology of α-Mg dendrite of Mg-5-wt% Zn alloy under isothermal solidification at $t = 6000\Delta t$ on (c) $\{0001\}$ crystal plane and (d) $\{11\bar{2}1\}$ crystal plane.

5. Conclusions

In this study, parameter calculation and result storage for phase-field simulation in α-Mg dendrite growth of Mg-5-wt% Zn alloy is investigated. The main conclusions are as follows.

(i) Key parameters of the phase-field model, such as equilibrium partition coefficient k, liquidus slope m, solutal diffusion coefficient in liquid D_l, and solutal diffusion coefficient in solid D_s are obtained through the phase diagram and empirical formulas.

(ii) Both the structured grid method and the structured point method can be used to store simulation results. Moreover, using the structured point storage method will reduce about 60% storage space and 37.5% storage time compared with the structured grid storage method.

(iii) The convergent simulation results of α-Mg dendrite growth are obtained and in good agreement with the optical micrograph of experimental results, verifying the accuracy of parameters and stability of storage methods.

Acknowledgements

Project supported by the National Natural Science Foundation of China (Grant Nos. 52074246, 52275390, 52205429, and 52201146), the National Defense Basic Scientific Research Program of China (Grant Nos. JCKY2020408B002 and WDZC2022-12), the Science and Technology Major Project of Shanxi Province, China (Grant Nos. 20191102008 and 20191102007), and the Guiding Local Science and Technology Development Projects by the Central Government, China (Grant Nos. YDZJSX2022A025 and YDZJSX2021A027).

References

[1] Chen L Q and Zhao Y H 2022 *Prog. Mater. Sci.* **124** 100868
[2] Geslin P A, Chen C H, Tabrizi A M and Karma A 2021 *Acta Mater.* **202** 42
[3] Chen C H, Tabrizi A M, Geslin P A and Karma A 2021 *Acta Mater.* **202** 463
[4] Xin T Z, Zhao Y H, Mahjoub R, Jiang J X, Yadav A, Nomoto K, Niu R M, Tang S, Ji F, Quadir Z, Miskovic D, Daniels J, Xu W Q, Liao X Z, Chen L Q, Hagihara K, Li X Y, Ringer S and Ferry M 2021 *Sci. Adv.* **7** eabf3039
[5] Zhao Y H 2022 *Intermetallics* **144** 107528
[6] Zhao Y H, Liu K X, Hou H and Chen L Q 2022 *Mater. Design* **216** 110555
[7] He R, Wang M T, Jin J F and Zong Y P 2017 *Chin. Phys. B* **26** 128201
[8] Zhao Y H 2023 *Front. Mater.* **10** 1145833
[9] Ohno M, Shibuta Y and Takaki T 2019 *Mater. Trans.* **60** 170
[10] Zhang A, Guo Z P, Jiang B, Du J L, Wang C H, Huang G S, Zhang D F, Liu F, Xiong S M and Pan F S 2021 *Acta Mater.* **214** 117005
[11] Wang N Q, Korba D, Liu Z X, Prabhu R, Priddy M W, Yang S F, Chen L and Li L K 2021 *Comput. Methods Appl. Mech. Engrg.* **385** 114026
[12] Greenwood M, Shampur K N, Ofori-Opoku N, Pinomaa T, Wang L, Gurevich S and Provatas N 2018 *Comp. Mater. Sci.* **142** 153
[13] Sakane S, Aoki T and Takaki T 2022 *Comp. Mater. Sci.* **211** 111507
[14] Guo Y Q, Luo S, Wang W L and Zhu M Y 2022 *J. Mater. Res. Technol.* **17** 2059
[15] Sun W Z, Yan R, Zhang Y Z, Dong H B and Jing T 2019 *Comp. Mater. Sci.* **160** 149
[16] Zhang Z D, Cao Y T, Sun D K, Xing H, Wang J C and Ni Z H 2020 *Chin. Phys. B* **29** 028103
[17] Xing H, An Q, Dong X L and Han Y S 2022 *Chin. Phys. B* **31** 048104
[18] Zhu C S, Gao Z H, Lei P, Feng L and Zhao B R 2022 *Chin. Phys. B* **31** 068102
[19] Tourret D, Liu H and Llorca J 2022 *Prog. Mater. Sci.* **123** 100810
[20] Chen Q Q, Zhang L, Tang S, Liang C P, Ma Y Z and Liu W S 2021 *Calphad* **74** 102271
[21] Chen W P, Zhao Y H, Yang S, Zhang D and Hou H 2021 *Adv. Compos. Hybrid Mater.* **4** 371
[22] Zhao Y H 2023 *Npj Comput. Mater.* **9** 94
[23] Yamada R, Kudo M, Kim G, Takaki T, Shibuta Y and Ohno M 2022 *Comp. Mater. Sci.* **204** 111173
[24] Sun W Z, Xie Y, Yan R, Ma S D, Dong H B and Jing T 2019 *Metall. Mater. Trans. B* **50** 2487
[25] Echebarria B, Folch R, Karma A and Plapp M 2004 *Phys. Rev. E* **70** 061604
[26] Ohno M and Matsuura K 2009 *Phys. Rev. E* **79** 031603
[27] Du J L, Zhang A, Guo Z P, Yang M H, Li M, Liu F and Xiong S M 2018 *Acta Mater.* **161** 35
[28] Xing H, Dong X L, Wang J Y and Jin K X 2018 *Metall. Mater. Trans. B* **49** 1547
[29] Boukellal A K, Rouby M and Debierre J M 2021 *Comp. Mater. Sci.* **186** 110051
[30] Ouyang Y F, Liu K, Peng C Y, Chen H M, Tao X M and Du Y 2019 *Calphad* **65** 204
[31] Zhong W and Zhao J C 2017 *Metall. Mater. Trans. A* **48** 5778
[32] Yang S, Su X P, Wang J H, Yin F C, Tang N Y, Li Z, Wang X M, Zhu Z X, Tu H and Li X Q 2011 *Metall. Mater. Trans. A* **42** 1785
[33] Becker M, Dantzig J, Kolbe M, Wiese S T and Kargl F 2019 *Acta Mater.* **165** 666
[34] Du J L, Zhang A, Guo Z P, Yang M H, Li M and Xiong S M 2017 *Acs Omega* **2** 8803
[35] Gale W F and Totemeier T C 2004 *Smithells Metals Reference Book*, 8nd edn. (Oxford: Butterworth–Heinemann) pp. 8-2–14-1
[36] Kammerer C C, Kulkarni N S, Warmack R J and Sohn Y H 2014 *J. Alloys Compd.* **617** 968